Interferometric sensing platform with dielectric nanostructured thin films

Celo, D.; Post, E.; Summers, M.; Smy, T.; Brett, M. J.; Albert, J.

National Research Council Canada   Conseil national de recherches Canada

Canada

Interferometric sensing platform with dielectric nanostructured thin films

D. Celo[1*], E. Post[2], M. Summers[3], T. Smy[1], M.J. Brett[3], and J. Albert[1]

[1]Carleton University, Department of Electronics, 1125 Colonel By Drive,
Ottawa, ON, K1S 5B6 Canada
[2]The Institute for Microstructural Sciences, National Research Council,
Ottawa, ON, Canada K1A 0R6
[3]National Institute for Nanotechnology, National Research Council,
Edmonton, AB, Canada T6G 2M9
* Corresponding author: dcelo@doe.carleton.ca

Abstract: A new interferometer-based optical sensing platform with nanostructured thin films of ZrO_2 or TiO_2 as sensing environment has been developed. With the application of an IC compatible Si_3N_4 waveguide technology, Mach-Zehnder interferometer devices have been fabricated. The application of the glancing angle deposition technique allowed fabrication of nanostructured thin films as the optical sensing environment. Sensing ability of fabricated devices has been demonstrated through the refractive index measurement of a known gas. The transmission spectra and time response measurements have demonstrated a maximum phase shift of $\Delta\varphi=\pi/10$ and a $|\Delta P_{out}|=0.65$ dBm. Devices with TiO_2 film on the sensing region performed much better than devices with ZrO_2, with sensitivity twice as high.

OCIS codes: (130.0130) Integrated optics; (130.6010) Sensors

References and links

1. P. V. Lambeck, "Integrated optical sensors for the chemical domain," Meas. Sci. Technol. **17**, R93-R116 (2006).
2. L. M. Lechuga, F. Prieto, and B. Sepulveda, in *Optical Sensors for Industrial and Environmental Application*s, (Springer, 2003).
3. J. van Lith, P. V. Lambeck, J. W. Hoekstra, R. G. Heideman, and R. R. Wijn, "The segmented waveguide sensor: principle and experiments," J. Lightwave Technol. **23**, 355-363 (2005).
4. S. Létant and M. J. Sailor, "Detection of HF gas with a porous Si interferometer," Adv. Mater. **12**, 355-359 (2000).
5. K. Robbie, L .J. Friedrich, and S. K. Dew, "Fabrication of thin films with high porous nanostructure," J. Vac. Sci. Technol. A **13**, 1032-1035 (1995).
6. J. Steele, A. van Popta, M. Hawkeyea, J. Sit, and M. Brett, "Nanostructured gradient index optical filter for high-speed humidity sensing," Sens. and Actuators B **120**, 213–219 (2006).
7. K. Harris, A. Huzinga, and M. Brett, "High-speed porous thin film humidity sensors," Electrochem. Solid-State Lett. **5**, H27– H29 (2002).
8. S. Hsu and Y. Huang, "A novel Mach-Zehnder interferometer based on dual arrow structures for sensing applications," J. Lightwave Technol. **23**, 4200–4206 (2005).
9. R. N. Fabricius, G. Gauglitz, and J. Ingenhoff, "A gas sensor based on an integrated optical Mach-Zehnder interferometer," Sens. and Actuators B, **7**, 672-676 (1992).
10. R. Ramaswami and K. N. Sivarajan, in *Optical Networks: A Practical Perspective*, Second ed., (Morgan Kaufmann, 2002).
11. G. J. Valdhuis, O. Parriaux, H. J. Hoekstra, and P. V. Lambeck, "Sensitivity enhancement in evanescent optical waveguide sensors," J. Lightwave Technol. **18**, 677-682 (2000).
12. Optiwave, "Waveguide Optics Modeling Software Systems," in *OptiBPM Technical Background,* Ottawa, ON, Canada, (2005).
13. A. Dakka, J. Lafait, C. Sella, S. Berthier, J. C. Martin, and M. Maaza, "Optical properties of Ag–TiO2 nanocermet films prepared by cosputtering and multilayer deposition techniques," Appl. Opt. **39**, 2745-2753 (2000).

14. M. W. McCall and A. Lakhatakia, "Integrated optical polarization filtration via sculptured-thin-film technology," J. Mod. Opt. **48**, 2179-2184 (2001).
15. B. Dick and M. J. Brett, "Nanofabrication by glancing angle deposition," Encyclopedia of Nanoscience and Nanotechnology, **6**, 703-725 (2004).
16. D. Celo, R. Vandusen, T. Smy, J. Albert, N. G. Tarr, and P. D. Waldron, "Low temperature plasma etching for Si_3N_4 waveguide applications," J. Vac. Sci. Technol. A **26**, 253-258 (2008).
17. A. C. van Popta, J. Cheng, J. C. Sit, and M. J. Brett, "Birefringence enhancement in annealed TiO_2 thin films," J. Appl. Phys. **102**, 013517 (2007).
18. G. Gulen and M. N. Inci, "Thermal optical properties of TiO_2 films," Opt. Mater. **18,** 373-381 (2002).
19. E. Drouard, P. Huguet-Chantome, L. Escoubas, and F. Flory, "$\Delta n/\Delta T$ measurements performed with guided waves and their application to the temperature sensitivity of wavelength-division multiplexing filters," Appl. Opt. **41**, 3132-3136 (2002).
20. E. Hecht, *Optics*, (Addison Wesley Longman, Inc., Third ed., 1998).

1. Introduction

During the last decade, a need for faster and better means of detection, communication, and data processing has encouraged rapid growth on the field of all-optical components. This has led to the development of a variety of new optical sensing devices able to detect a measurand and process data using electromagnetic energy. From the wide range of integrated optical sensors, devices based on interferometric homogenous sensing have been successfully developed [1]. While some good sensitivities are reported [2, 3], there are limiting factors inherited to the existing methodology of device design and fabrication. A large refractive index difference at the waveguide core-measurand boundary causes: (a) the mode propagating into the waveguide to be strictly confined inside the core region, resulting in a very small evanescent field portion, (b) the evanescent field traveling into the sensing area experiences high absorption and scattering losses, and (c) increases Fresnel reflection losses at the boundaries, leading to a potential interference of the reflected power with the evanescent filed.

A possible solution to these problems would be a sensing environment with strictly controlled refractive index, porosity, structural configuration and high surface area to volume ratio. While similar structures using porous materials have been fabricated from other research groups [4], the application of thin films fabricated with the glancing angle deposition (GLAD) technique [5] offers a high degree of control over the film nanostructure. The porous nature of sensing layer makes the device sensitive to the voids environment; as it propagates along the film, the evanescent field drawn deep into the porous layer probes the environment. The limited interaction of the evanescent field with the sensitive cladding is compensated by the long propagating distance. Furthermore, this technology allows the development of a so-called sensor platform [1], which with minor modifications can be tailored to a large variety of optical sensing devices. By changing very few deposition parameters such as flux incidence angle or angular velocity of substrate rotation, a broad range of nanostructured thin films (NTF) specific to individual applications can be created [6, 7].

The capability of the proposed sensing platform for refractive index measurement is demonstrated in this work. The design aspects briefly address the rationale behind the use of interferometric sensing with a Mach-Zehnder interferometer (MZI). The effect of core-cladding refractive index on the modal sensitivity is simulated, with results suggesting that good optical sensitivity can be achieved with devices based on silicon nitride (Si_3N_4) waveguides and zirconia (ZrO_2) or titania (TiO_2) NTF deposited on the sensing region. Processing and fabrication section summarizes waveguide fabrication steps and the application of GLAD technology for deposition of dielectric NTFs of slanted columns. Finally, the optical sensing ability of fabricated devices is demonstrated through the refractive index measurement of a known gas.

2. Design considerations

The advantage of the MZI in various interferometric sensing applications [8, 9] is based on the ability to control the optical path difference between arms by changing the refractive index

in one of them. Any refractive index change in one arm will strongly affect the output intensity. As schematically shown in Fig. 1, by locally removing the cladding layer in the sensing region, an interaction between the evanescent field of propagating mode and the material to be sensed can be achieved.
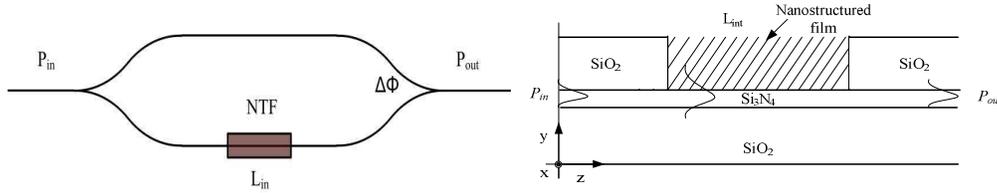

Fig. 1. Schematic representation of interferometric sensing (a) a MZI with sensing region in the lower arm, and (b) a magnified sectional view of sensing region depicting waveguide layers and NTF deposited on the opening.

For a single mode condition in the waveguide, the transfer function of the MZI can be seen as a sinusoidal function of $\Delta\varphi$ [10], with the quadrature points occurring when the phase difference between the two arms of the interferometer is $\Delta\varphi = (m+1/2)\pi$, for $m=0,1,2,...$ For a given transfer function of a MZI, the effective refractive index change ΔN_{eff} induced by the refractive index change within the evanescent field region can be obtained with:

$$\Delta\varphi = \frac{2\pi}{\lambda_0} L_{\text{int}} \Delta N_{eff} \tag{1}$$

where λ_0 is the wavelength of light in free space and L_{int} is the interaction length as shown in Fig. 1. With this relation, the actual ΔN_{eff} can be estimated by measuring the change in the fringe period of MZI transfer function. Similarly, Eq. (1) can be used to approximate the actual path length difference in between arms of an unbalanced MZI.

It is generally assumed that the sensitivity of a guided wave to changes of the cladding index is smaller or much smaller than that of a free-space beam [11]. This is based on the fact that only a small fraction of the optical field guided in the waveguide propagates in the sensing medium. In this context, the modal sensitivity (S_m) can be defined as the ratio of the effective refractive index change of the guided mode to the refractive index change (Δn_{SL}) of the cladding layer.

$$S_m = \frac{\Delta N_{eff}}{\Delta n_{SL}} \tag{2}$$

Using a mode solver [12], the guided mode effective index of a Si_3N_4 rib waveguide with refractive index $n=1.92$ and thickness $t=1$ µm, and SiO_2 buffer of $n=1.46$ and $t=3.5$ µm was simulated for a range of sensing layer refractive index values, with results plotted in Fig. 2.

As the graph shows, higher sensitivities can be achieved when core-cladding refractive indices get closer; of course, it becomes easier to pull the evanescent field outside the core layer deep into the cladding, where very little change in the cladding refractive index would strongly affect the field distribution inside the waveguide. Therefore a problem arises when we attempt to measure small refractive index changes in low index media (gases and aqueous liquids). With NTFs however, it is possible to achieve high index "average" cladding index, even with porous structures that can be infiltrated by substances to be measured. Small core-cladding refractive index difference can be achieved with ZrO_2 and TiO_2 NTF deposited on the sensing layer. Their relatively high refractive index, low absorption coefficient and a high transparency in the visible and near-IR region [13] make these dielectric materials suitable for the purpose.
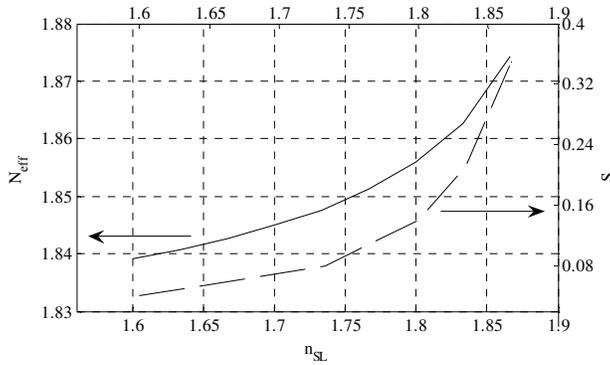
Fig. 2. Waveguide effective refractive index as function of cladding refractive index and simulated modal sensitivity.

The application of the GLAD technique for film deposition makes possible a strict control of optical properties [14], refractive index, porosity, structural configuration and high surface area to volume ratio. As shown in Ref. [5], this technique offers a high degree of control over the film microstructure. Porosity is created by enhanced self-shadowing during the growth process where a random growth fluctuation in one area produces a shadowed region where subsequent incident flux cannot reach and a high point where incident flux may deposit, creating preferred growth. By producing a symmetrical and highly oblique incident flux, shadowing can be greatly enhanced and highly porous films can be fabricated with vertical columns and porosities much greater than those fabricated with a one sided flux [15].

3. Fabrication

The procedure developed in Ref. [16] was adopted to fabricate Si_3N_4 waveguides and MZI devices with cross sectional dimensions and refractive indices shown in Fig. 3(a). A theoretical optimization completed on three layer stacks built from SiO_2 (n=1.456), Si_3N_4 (n=1.923) and gas (n in the range 1.0000-1.0010) have shown that the highest sensitivity parameter (S_m=0.0727) at wavelength λ=1.6 μm is obtained for a core layer thickness of 239 nm. At calculating the sensitivity such a layer stack is a good approximation for a channel waveguide with small etching depth, leading to the assumption that the application of a porous TiO_2 film will improve the device sensitivity. However, it should be noted that the cross sectional core dimensions of the chosen structure of Fig. 3(a) were not optimized for the highest sensitivity. The main criteria in selecting the core dimensions were the single mode behavior at wavelength 1620 nm and the mode confinement into the rib and evanescent part of the waveguide.

The layer thicknesses with corresponding refractive indices of a typical starting wafer are summarized in Table 1. After waveguide rib formation [Fig. 3(b)], a SiO_2 over-cladding layer of thickness 1.8 μm was deposited. Deposition was completed at low temperature (T=500°C) with atmospheric pressure chemical vapor deposition (APCVD) process in a conventional furnace with SiH_4 gas and O_2 oxidant.

Etching the SiO_2 over-cladding to create sensing wells was the next step in the process. Sensing windows for subsequent NTF deposition were patterned, with openings of size 24 μm wide by 2-4 mm long aligned with one of the arms of the balanced MZIs. Wet etching with siloxide etchant was applied, giving the necessary etch control for deposited SiO_2 films. It offers: (a) isotropic etching, avoiding vertical steps in the sensing wells, thus allowing a columnar film to be deposited, and (b) high etch selectivity of oxide over mask material and the underlying nitride. A microscope image of an etched wafer depicting sensing regions of three different lengths is shown in Fig. 4(a).
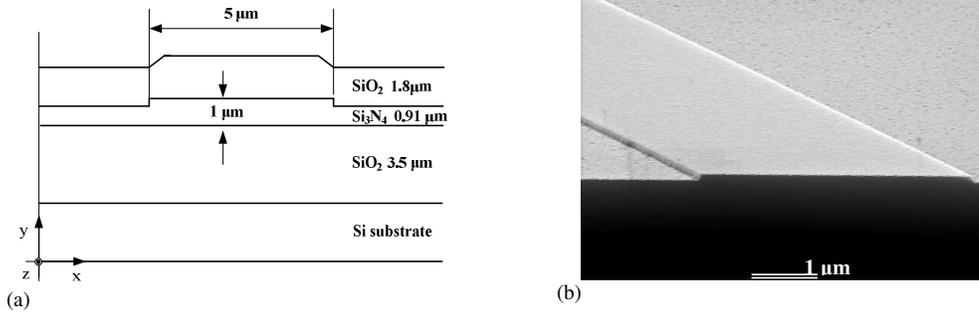
Fig. 3. The waveguide rib structure (a) a cross-sectional schematic representation, and (b) SEM image of a fabricated waveguide, showing the Si_3N_4 rib before deposition of SiO_2 cladding.

Table 1. Starting wafer parameters

Parameter	SiO_2 buffer	Si_3N_4	SiO_2 cladding
t (nm)	3510	1022	1830
n (λ=650 nm)	1.471	1.947	1.448
n (λ=1551 nm)	1.456	1.923	1.437

The NTF deposition process of source materials (99.7% pure ZrO_2 and 99.9% pure Ti_3O_5 supplied by Cerac Inc.) was completed onto unheated stationary processed wafers. The source to substrate distance of 43 cm and the flux incidence angle set at 85.0±0.1° resulted in porous films with tilted columns at β=45° with the wafer surface, pore volume fraction of 66 %, and refractive indices 1.44 and 1.51 corresponding to ZrO_2 and TiO_2. An image of a TiO_2 film of thickness 1.12 µm deposited on a stationary wafer was taken with a Hitachi S-4800 field emission scanning electron microscope (FE-SEM), and is shown in Fig. 4(b).
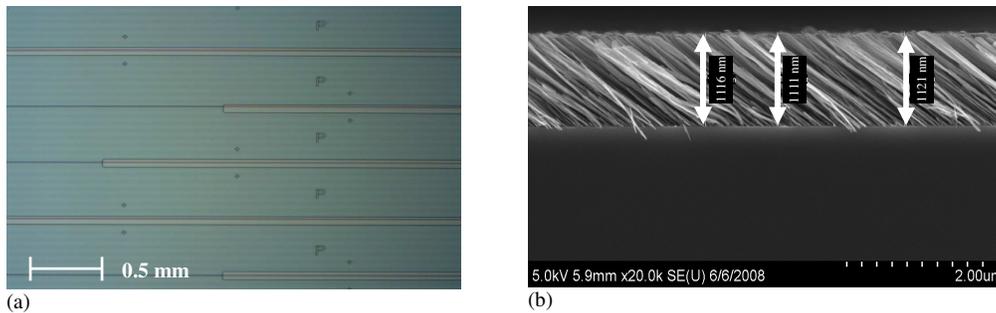

Fig. 4. Sensing windows and TiO_2 thin film structure (a) microscope image of a processed wafer depicting sensing windows where, SiO_2 layer has been etched, and (b) SEM image of a typical film deposited onto stationary processed wafer.

Evaporated thin films of both materials tend to be oxygen deficient. Previous studies [17] have found that an annealing process at a low temperature for an extended period improves film optical properties and crystalline structure. For this reason, deposited films were oxidized in a furnace for 12 hours at 100°C.

Therefore, after completing all the fabrication steps, the final sensor structure is similar to the MZI schematically shown in Fig. 1, where NTF of ZrO_2 or TiO_2 with thickness 1.1 µm and 45° tilted columns, similar to Fig. 4(b), are deposited in the sensing window of length 3.6 mm. As a result, such sensing devices are considered in the following measurements.

4. Experimental setup

A schematic of the measurement setup is shown in Fig. 5. An Agilent Lightwave Measurement System 8164B with tunable laser source module 81600B 200 was used as the light source. The signal from the laser source is transmitted through a single mode polarization-maintaining (PM) fiber into a polarization rotator controller which manipulates and controls the state of polarization of the input beam of light and couples the adjusted light into an output fiber. This polarization controller consisted on three components, a polarizing glass filter for transverse electric (TE) or transverse magnetic (TM) polarized light output, a half-wave plate, and an output coupler with fiber pigtail. The half wave plate position is controlled by a universal motor controller/driver (ESP 300 by NewPort) via a stepper motor, to allow precise and repeatable polarization rotation for TE or TM selection. It also allows the alignment of light as closely to the proper PM fiber axis as possible, thus maintaining the state of linear polarization and orientation of light along one of principal transmission axes within the output fiber.

A single mode PM tapered fiber was used to transmit the linearly polarized optical signal from polarization controller output into the device under test (DUT). Butt-coupling of fiber end to the waveguide facet provides good efficiency and mode matching ability, ensuing minimum coupling losses. The output light from the sample is collected using a 20x objective lens and passed through an analyzer consisting of a broad-band polarizer and a polarizing cube beam-splitter which splits the beam into two orthogonal, linearly polarized components. The output power is directed and measured with an Agilent 81624B InGaAs detector, or reflected (through a mirror) to an infra-red camera for visual inspection and alignment facilitation. The position of the input tapered fiber and the output lens can be controlled with individual stages, whereas the sample can securely be placed in a vacuum controlled stage, providing steadiness during the measurement process. Wavelength and/or time response measurements were run by LabView software.
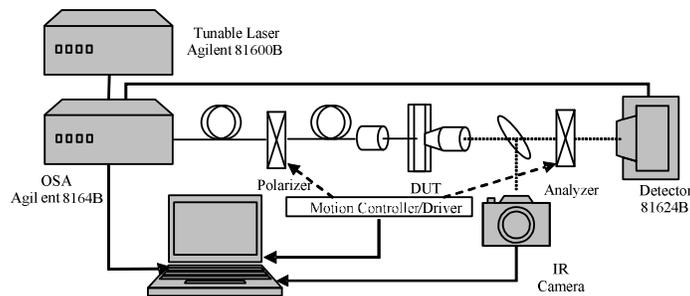

Fig. 5. Optical measurement setup at NRC optical testing laboratory.

In addition to the optical measurement system, a gas flow system able to create a gas environment surrounding the sensing arm of the MZI was created. A schematic of the gas flow system utilized to measure the refractive index of a known gas is shown in Fig. 6(a). To control the gas environment surrounding the MZI sensing arm, an acrylic cell with dimensions $10x15x10$ mm^3 was attached to the chip surface [Fig. 6(b)], with a double sided adhesive tape. A gas leak test completed on a dummy silicon wafer demonstrated the capability of this attachment method. Flexible tubing connected to the input hose barb on the gas cell supplied gas inside the cell. Gas flow control was achieved with a three port switch, a needle valve, and a pressure regulator connected at each gas line, permitting identical flow rates for both gasses. Gas cylinders of compressed nitrogen 99.998% purity (reference gas) and carbon dioxide 99.995% purity supplied the gas to the cell.
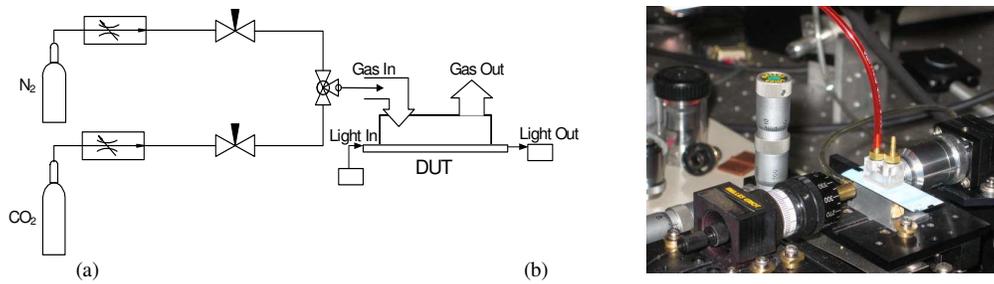
Fig. 6. Experimental setup for N_2 and CO_2 refractive index measurement (a) schematic representation of the system, and (b) photographed image of a waveguide substrate with an acrylic gas cell attached to the surface.

Before completing any optical measurement, the temperature change inside the cell due to the gas flow was measured. A type K thermocouple probe from OMEGA Corp. of diameter 0.25 mm was inserted inside the cell through the output barb. Thermocouple wires were connected to the hand-held unit (OMEGA HH802U), allowing temperature readings as gas flows inside the cell. Air temperature inside the cell with and without gas flow was measured, revealing a maximum temperature difference $\Delta T_{max} \leq 0.2°C$. With thermo-optic coefficients $\partial n/\partial T = -(1.77\pm0.7)10^{-4}$ K^{-1} [18] for TiO_2 and $\partial n/\partial T = (3\pm0.5)10^{-5}$ K^{-1} [19] for ZrO_2, the change in effective refractive index due to temperature is expected to induce a maximum phase shift $\Delta\varphi = 0.01\pi$. Therefore, the maximum shift in the interferometer output spectrum induced by the thermal variations in the measuring environment is significantly lower than the shifts predicted by simulation results, demonstrating that the gas flow does not change the ambient temperature significantly and therefore cannot be held responsible for the measured changes shown below. This conclusion is further supported by the presence of the Si substrate; its high thermal conductivity provides a good heat sink, thus contributing to a uniform temperature distribution in the MZI arms.

5. Results and discussion

As the gas flows into the cell, the environment surrounding the sensitive layer changes accordingly, resulting in a refractive index change within the evanescent field region. With relation of Eq. (1), the refractive index change affects the N_{eff} and induces a phase shift $\Delta\varphi$ in the MZI transfer function. As a result, the transfer function $P_{out} = f(\lambda)$, will shift accordingly, reflecting any change in the sensing environment. Measuring this $\Delta\varphi$ after introducing a new gas into the cell gives the ability to determine Δn and gas refractive index.

Measurements were completed on fabricated devices with ZrO_2 or TiO_2 NTF deposited in the sensing window. The gas content into the cell was alternated from N_2 (the reference) to CO_2 in five minute intervals and transmittance for TE polarized light was measured at each interval. A least squares regression procedure to fit a mathematical expression for the transmission power of an unbalanced MZI and the filtered experimental modulation waveform was completed with results shown in Fig. 7. Fitting parameters such as the square of the correlation coefficient (R^2) and the chi-square distribution (*Chisq*) are summarized in Table 2. The wavelength response of the MZI is shifted due to gas content change in the sensing environment. At temperature 0°C and pressure 1 atm the difference in refractive index between N_2 and CO_2 is approximately $\Delta n = 1.57e-4$ refractive index units (RIU) [20]. Since both gases undergo the same temperature increase, this Δn is expected to be true even at room temperature, when the measurements were completed. Due to this Δn, the output intensity of the MZI shifts by $\pi/16$ and $\pi/10$ respectively for devices with ZrO_2 and TiO_2.
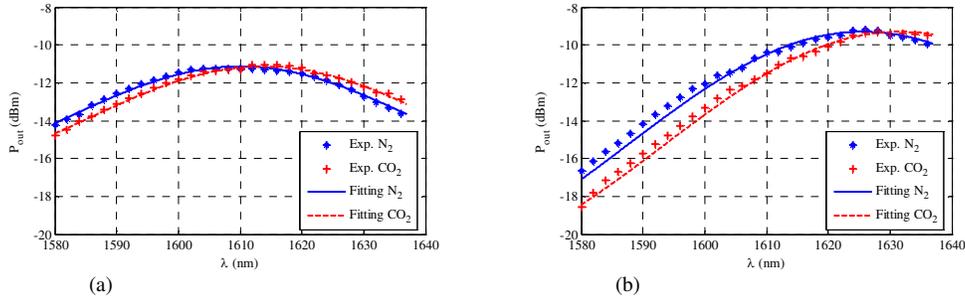
Fig. 7. Output power of MZI with N_2 and CO_2 in sensing environment for (a) device with ZrO_2, and (b) device with TiO_2 film deposited on the sensing arm.

Table 2. Fitting parameters for graphs of Fig. 7.

Device	Gas environment	R^2	$Chisq$
ZrO_2	N_2	0.9943	0.1367
	CO_2	0.9942	0.0871
TiO_2	N_2	0.9958	0.6347
	CO_2	0.9977	0.5594

Knowing the phase shift $\Delta\varphi$, the effective index change ΔN_{eff}, and the corresponding refractive index change Δn (Fig. 8), the slope of the sensitivity curve ($S = \Delta N_{eff}/\Delta n$) is calculated, with results shown in Table 3. Note that the sensitivity S is defined with respect to the infiltrated gas refractive index change Δn, and is different from the modal sensitivity S_m defined above with respect to the change of the average cladding index (porous film plus gas). Without the porous structure, S becomes equal to S_m and hence would be negligibly small for gas refractive indices. The error bars around the experimental points take into account the error introduced by the curve fitting procedure and the noise associated with the measured signal; they correspond to one standard deviation of ΔN_{eff} calculated from data sets representing three repeated measurements.
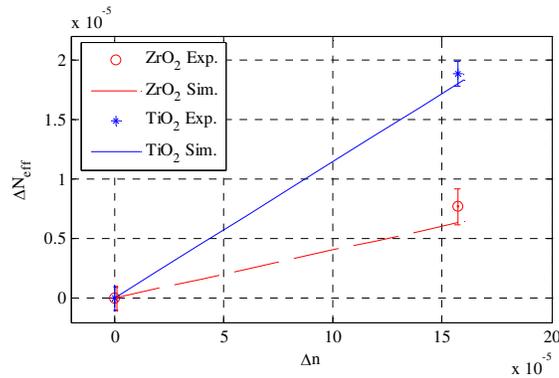

Fig. 8. Sensitivity comparison for devices with ZrO_2 and TiO_2 film on the sensing layer.

For comparison, MZI simulated sensitivities obtained for structures similar to the one shown in Fig. 1, with an "effective" cladding layer refractive index 1.42 and 1.51 in the sensing window (corresponding to ZrO_2 and TiO_2 GLAD films), and the waveguide cross sectional dimensions and refractive indices given in Fig. 3(a), are shown in Fig. 8. A Δn from

0 to 16e-5 in ten steps produces linear responses, with higher slope obtained for device with TiO_2 in the sensing window.

Both experimental and simulated results of Fig. 8 are in a good agreement; higher sensitivity has been achieved by the device with TiO_2 film. As predicted by the modal sensitivity curve of Fig. 2, a higher refractive index of sensing layer shifts the device operation point toward a higher slope region, thus providing better sensing abilities. Experimental results demonstrate that sensitivity is strongly affected by the core-cladding refractive index difference. Of course, this presents an important aspect of this optical sensing platform: any suitable arrangement of a dielectric structured thin film with a planar waveguide may result in an optical sensing device and, hence, adjustments on the sensing layer refractive index will enhance sensitivity of the device.

Table 3. The slope of the sensitivity curve for devices with ZrO_2 and TiO_2.

Device	$\Delta\varphi$	ΔN_{eff}	S
ZrO2	$\pi/16$	7.6705e-6	0.0489
TiO2	$\pi/10$	1.8837e-5	0.1200

Time response of a MZI output can also be employed for refractive index determination. This measurement encounters the time response of porous cladding, and the gas system (the chemical formation inside the cell is changing gradually as a result of its cross sectional dimensions being different from those of the input gas pipe). Measurements were completed for TE polarized light at λ=1620 nm. As a result, devices will operate on the linear part of the transfer function, where any change in the refractive index value corresponds to a change in power output. Time response was measured for alternating N_2 and CO_2 gas flow on the sensing environment. After filtering out the high frequency noise coupled with the signal, the measured time response of devices with ZrO_2 and TiO_2 is shown in Fig. 9.
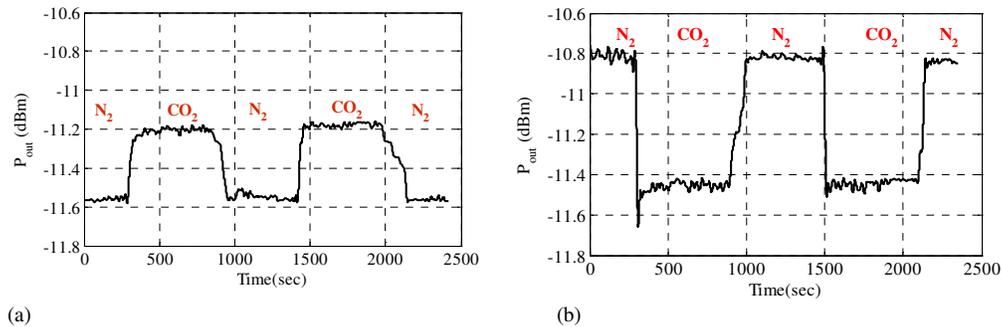

(a)   (b)

Fig. 9. Time response for alternating N_2 and CO_2 in the gas cell, device with (a) ZrO_2, and (b) TiO_2 film.

While the output time response patterns of Fig. 9 look similar in both devices, there is a quantitative difference. When CO_2 is introduced in the sensing environment, the output signal of the device with ZrO_2 film is increase by 0.38 dBm. In contrast, the output signal of the device with TiO_2 film decreases by 0.65 dBm. While the sine of ΔP_{out} depends on the wavelength of operation and has no significance for sensitivity evaluation, its absolute value is a clear indication that devices with TiO_2 can achieve higher sensitivities. As demonstrated, $|\Delta P_{out}|$ for a device with TiO_2 is almost twice that of a device with ZrO_2, for the same Δn, which is in complete agreement with results of Fig. 8.

Also, looking at the time response plots, a qualitative observation can be drawn. While the output power changes instantly when switching from N_2 to CO_2, there is a time constant when switching from CO_2 to N_2. It takes approximately 200 s to fill the 1.2 μm thick NTF with N_2

but only 80 s to replace it with CO_2. This could be due to a higher density, and/or a higher sticking coefficient of CO_2 as compared to N_2. Note here that sticking coefficient is a parameter used in surface physics to describe the ratio of the number of molecules that do absorb to a surface to the total number of atoms that impinge upon that surface during the same period of time. However, in order to fully understand this phenomenon, further investigations would be required. In general, a more porous film would result in faster exchange times, addressing the time constant issue, but at the expense of sensitivity because of the lowering of the effective NTF refractive index.

6. Conclusion

A new sensing platform for highly efficient optical sensing based on dielectric material NTF as sensing environment has been presented. By changing very few deposition parameters such as flux incidence angle or angular velocity of substrate rotation, a broad range of NTFs specific to individual applications can be created. Sensing ability of this new platform was demonstrated through design, fabrication, and characterization of interferometer-based devices with ZrO_2 or TiO_2 NTF as sensing environment. Sensitivity of fabricated devices was experimentally confirmed with the refractive index measurement of a known gas. By alternating gas content in the sensing environment and measuring the frequency response, a maximum phase shift of $\varphi=\pi/10$ on the MZI transmission spectra was achieved. Devices with TiO_2 film deposited on the sensing area performed much better than devices with ZrO_2, with sensitivity twice as high, demonstrating an important aspect of this optical sensing platform: any suitable arrangement of a dielectric structured thin film with a planar waveguide may result in an optical sensing device.

Acknowledgment